Modeling damage and deformation in impact simulations

Gareth S. COLLINS,[1*] H. Jay MELOSH,[1] and Boris A. IVANOV[2]

[1]Lunar and Planetary Laboratory, University of Arizona, Tucson, Arizona 85721, USA
[2]Institute for Dynamics of Geospheres, Russian Academy of Sciences, Moscow, Russia 119334
[*]Corresponding author. E-mail: gareth@lpl.arizona.edu

Abstract–Numerical modeling is a powerful tool for investigating the formation of large impact craters but is one that must be validated with observational evidence. Quantitative analysis of damage and deformation in the target surrounding an impact event provides a promising means of validation for numerical models of terrestrial impact craters, particularly in cases where the final pristine crater morphology is ambiguous or unknown. In this paper, we discuss the aspects of the behavior of brittle materials important for the accurate simulation of damage and deformation surrounding an impact event and the care required to interpret the results. We demonstrate this with an example simulation of an impact into a terrestrial, granite target that produces a 10 km-diameter transient crater. The results of the simulation are shown in terms of damage (a scalar quantity that reflects the totality of fragmentation) and plastic strain, both *total* plastic strain (the accumulated amount of permanent shear deformation, regardless of the sense of shear) and *net* plastic strain (the amount of permanent shear deformation where the sense of shear is accounted for). Damage and plastic strain are both greatest close to the impact site and decline with radial distance. However, the reversal in flow patterns from the downward and outward excavation flow to the inward and upward collapse flow implies that net plastic strains may be significantly lower than total plastic strains. Plastic strain in brittle rocks is very heterogeneous; however, continuum modeling requires that the deformation of the target during an impact event be described in terms of an average strain that applies over a large volume of rock (large compared to the spacing between individual zones of sliding). This paper demonstrates that model predictions of smooth average strain are entirely consistent with an actual strain concentrated along very narrow zones. Furthermore, we suggest that model predictions of total accumulated strain should correlate with observable variations in bulk density and seismic velocity.

INTRODUCTION

The formation of large impact craters is an important but poorly understood geologic process. The controversy surrounding current models is primarily associated with the late stages of the impact process—crater collapse. Crater collapse is the gravitationally driven modification of the cavity generated during the early stages of an impact event. It is the last major stage in the formation of an impact crater and has the most profound influence on the final morphology of the crater. For small "simple" craters, the collapse process is reasonably well-understood (Grieve et al. 1977; Melosh 1989): highly brecciated and molten rocks that were originally pushed out of the opening crater slide back down the steep crater walls, forming a melt-and-breccia lens at the base of the crater. The end result of this process is a shallow, bowl-shaped depression, where the average slope is at or below the angle of repose (about 30°). For complex craters, however, the details of the late-stage formation process are still unresolved (Melosh and Ivanov 1999) despite several decades of effort by geologists, geophysicists, experimentalists, and modelers alike.

The study of large impact crater formation is hindered by the scale and rarity of these events. There has been no direct observation of complex crater collapse in recorded history; large impact events are, fortunately, infrequent. In addition, the scale of experimental studies is somewhat inappropriate for drawing conclusions about the collapse of the largest craters in the solar system. The dominance of gravity in influencing the collapse stage of crater formation implies that, for the most part, the results of the small-scale laboratory collapse experiments cannot be extrapolated meaningfully to the scale of complex craters. Similarly, underground nuclear explosions, although extremely valuable in elucidating the

principal features of the excavation stage, are also not of an applicable scale. The two avenues for studying complex crater collapse that can be pursued are abstract computer simulation (Bjork 1961; O'Keefe and Ahrens 1993; Melosh and Ivanov 1999), which requires a detailed knowledge of all the relevant physics, and observational analysis of the scars left behind by the impact (Dence et al. 1977; Grieve et al. 1981; Lambert 1981; Spray 1998).

The path toward a complete understanding of how impact craters form must involve the integration of observation (throughout this paper, observation should be read to include experimental, geological, and geophysical observation) and numerical modeling. The realism of numerical models must be tested by validating model results with detailed observations. Consequently, there is a need to identify appropriate model results that can be used for validation. Fortunately, numerical models are, in one sense, the best instrumented experiment; any desirable variable may be recorded for any location within the crater and for all times throughout the crater formation process. However, the restrictions of computer power and time require that computer models be run with a resolution too coarse to accurately predict the thermodynamic or deformational history of a hand-sized rock sample. For these reasons, many previous numerical studies have used final crater morphology (for example, Wünneman and Ivanov 2003), or subsurface structure, inferred from borehole analysis, geologic outcrop, or geophysics (for example, Ivanov and Deutsch 1999; O'Keefe and Ahrens 1999; Collins et al. 2002) as quantitative tests of a code's success. For detailed simulation of terrestrial craters, however, none of these may be available, or useful, because impact craters on Earth are often heavily eroded or modified in some way. Furthermore, although geophysical surveys are extremely valuable tools for investigating the subsurface structure of an impact crater, the results that they provide are subject to interpretation and, thus, should be used carefully as a validation of model results.

An alternative validation technique, when considering terrestrial craters, is to compare the history of different parts of a numerical model in terms of one or more state variable (stress, strain, temperature, and so on) with corresponding parts of the eroded crater remnant. For example, Ivanov (2002) used measurements of peak shock pressure from drill core samples of the Puchezh-Katunki impact structure to validate peak shock pressure predictions from a numerical simulation. Unfortunately, data of this kind are often difficult to obtain because natural rock targets are extremely heterogeneous and, hence, respond non-uniformly to shock and deformation. Furthermore, many of the known terrestrial impact craters cannot provide the types of measurements required; they may be buried, heavily eroded and/or tectonically deformed.

One of the most promising means of comparing observation and numerical models is by quantifying damage

and deformation. Damage is a state variable now included in many codes used for simulation of impact events (Melosh et al. 1992; Ivanov et al. 1997; O'Keefe et al. 2001). It provides a measure of the degree of fracturing and, hence, the strength of the material within the cell. In its simplest form, it is merely the integrated plastic strain (for example, Johnson and Holmquist 1993); however, more sophisticated algorithms exist where damage is a function of the style and rate of deformation (Rubin et al. 2000). Deformation is quantified by strain, which is inherently monitored by all hydrocodes but seldom reported. In this paper, we present an analysis of damage and deformation around a mid-sized (10 km-diameter transient crater) terrestrial crater to illustrate what the current state-of-the-art computer codes used to study impact events predict for the post-impact state of the target. We find that, although particle motions within the target can move material large distances away from the impact point and back, the plastic shear strain experienced by the target exceeds 1 (100%) in only a small region surrounding the crater. For the most part, the target experiences strains on the order of 0.01–0.25 (1–25%). We also illustrate that the concept of damage in numerical models requires careful interpretation. We show that a cell with a damage of 1, when resolved in finer detail, can reflect heterogeneous damage. Hence, although numerical models predict that much of the target becomes "damaged" during the cratering process, the target rock within this zone will likely reflect a range of deformation features. It is our hope that the discussion contained within this paper will inspire further collaboration between geologists and modelers to accurately compare model results of deformation with field measurements of strain.

MODELING ROCK FAILURE AND DEFORMATION

Simulating deformation and failure of rock material in an impact event requires a sophisticated constitutive model. The constitutive model is a set of equations that approximates the observed behavior of rock materials when subjected to differential stress. For example, the stress at which rock begins to fail and how plastic deformation affects this critical stress. Laboratory rock mechanics experiments show that the critical stress at the onset of failure (yield strength) is a function of confining pressure, temperature, strain, strain rate, porosity, and sample size (for a recent review, see Lockner [1995]). Figure 1 shows several important concepts concerning the strength of rock material as a function of pressure. For fragmented rock materials, the shear strength is approximately linearly proportional to the confining pressure (Stesky et al. 1974; Byerlee 1978) where the constant of proportionality is known as the coefficient of friction (dashed line in Fig. 1a). In the absence of overburden pressure, fragmented rock materials have no strength. For intact rocks, on the other hand, there is a finite yield strength at zero pressure, termed the cohesion, and a tensile strength (represented by the negative x-
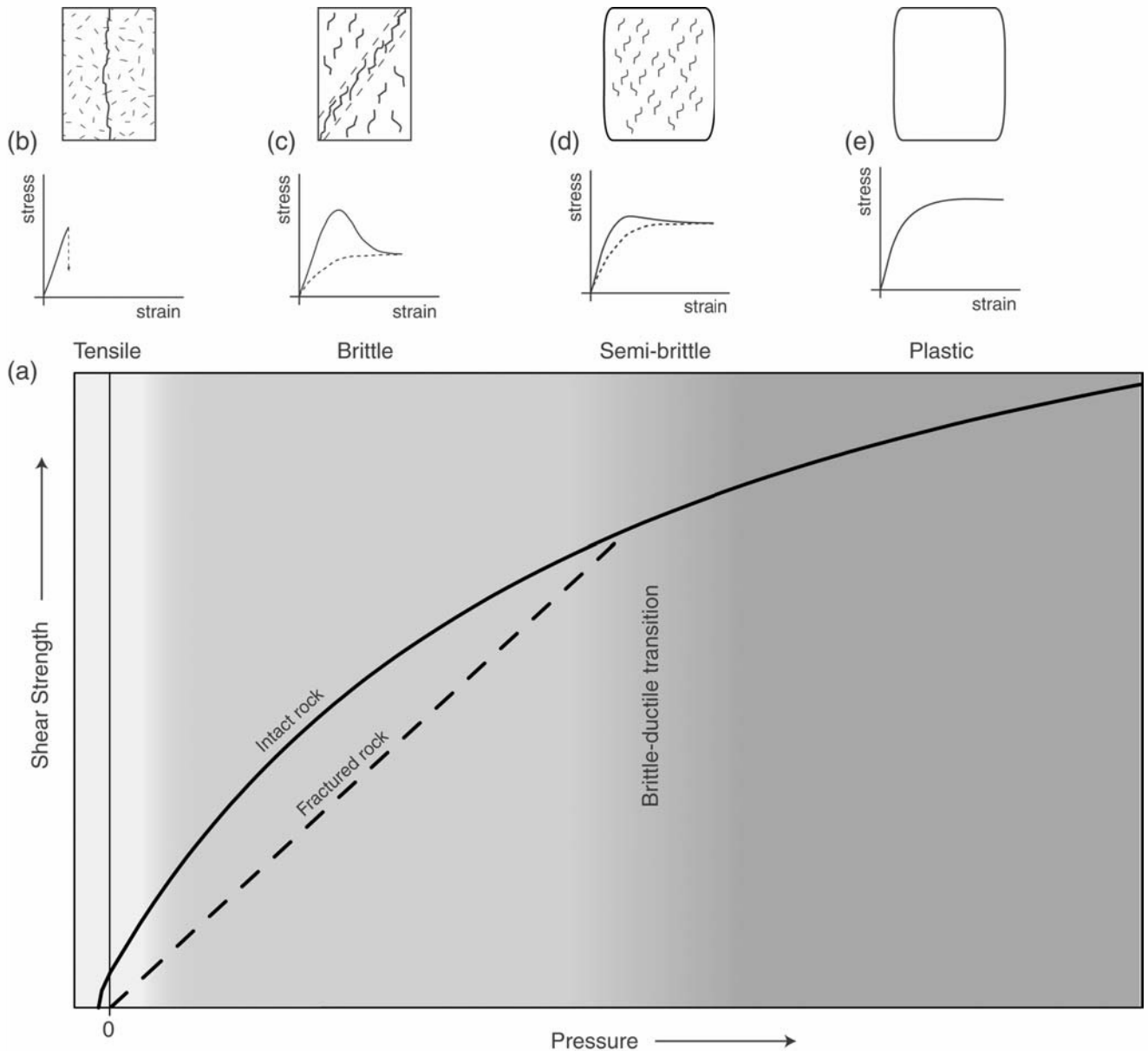
Fig. 1. The strength of rock materials as a function of pressure: (a) illustrates the typical relationship between shear strength and confining pressure for intact (solid line) and fractured (dashed line) rock material. The shading also illustrates the different regimes of deformation: tensile, brittle compressive, semi-brittle, and plastic; (b–e) illustrate the typical fracture patterns observed in laboratory-scale rock mechanics experiments (top panel; with maximum compressive stress in the vertical direction) and the associated stress strain curves for both intact rock (solid lines) and pre-fractured rock (dashed lines).

intercept for the solid curve in Fig. 1a). As pressure increases, the yield strength for intact rock rises; the local slope of the strength versus pressure curve is called the coefficient of internal friction. Lundborg (1968) found that a good, smooth approximation to rock mechanics data on shear strength versus pressure results from a formula where the coefficient of internal friction declines with increasing pressure (see Equation A2 in the Appendix); thus, at some large confining pressure, the shear strength reaches a constant value commonly called the von Mises plastic limit.

The strength of rock materials, both intact and fragmented, also decreases with increasing temperature. As temperature approaches the melting temperature, the resistance to shear declines steadily to zero at the melting point (see Equation A8 in the Appendix). In effect, the cohesion and the coefficient of friction are reduced by increasing temperature. Thus, for higher temperature conditions, the curves in Fig. 1a would be less steep, and the intact rock curve would be moved down.

Figure 1 illustrates that not only does the magnitude of

the strength increase with increasing confining pressure but also that the failure mechanism changes. At low temperatures and pressures, deformed rock masses respond to applied forces in a brittle manner. That is, deformation is not spread uniformly throughout the rock mass but is, instead, concentrated in narrow zones that separate largely intact regions (Figs. 1b and 1c). The ultimate reason for localization of deformation in this regime is that fractured rock (dashed line in Fig. 1a) is significantly weaker than intact rock (solid line in Fig. 1a). Thus, once a narrow zone of damaged rock is formed, it offers less resistance to sliding than the surrounding intact rocks, and further deformation of the rock mass occurs preferentially along these zones (Rice 1976). Whether this lowered resistance is already present in the rock in the form of pre-existing fractures (joints or faults) or whether it develops as a result of the global deformation itself is irrelevant for the final outcome.

Figures 1b and 1c illustrate stress versus applied strain for tensile and compressive failure of brittle rocks respectively. In both cases, as strain rises up to the elastic limit (typically less than a few percent), the stress rises monotonically with increasing strain. In the case of tensile failure, once the tensile strength of rock is exceeded, flaws in the sample tend to grow in the direction perpendicular to the maximum tension axis (Fig. 1b). These flaws concentrate the applied stress at their tips, thus increasing the effective stress across the remaining intact rock. Consequently, the development of these flaws perpetuates their own growth, resulting in a rapid, unstable path to complete failure (denoted by the sharp stress-drop in Fig. 1b).

In stark contrast, shear cracks cannot grow in their own plane. Thus, instead of the continued lengthening of a properly oriented tensile flaw, slip on a shear crack produces stress concentrations at its tips that initiate new cracks at a steep angle to the plane of the original crack (Horii and Nemat-Nasser 1986; Ashby and Sammis 1990). The new fractures propagate parallel to the most compressive stress axis and open as tensile fractures. The formation of the familiar inclined shear zone in rock mechanics experiments (Fig. 1c) seems to be the result of the growth of small flaws (mainly grain boundary and internal cleavage cracks), the linkage of the out-of-plane secondary cracks as they encounter one another, and their ultimate union into a complex, rough-surfaced band of shearing (Bombolakis 1973). Thus, for intact rocks, illustrated by the solid curve in Fig. 1c, the stress shows a peak followed by a more or less rapid decline to a residual stress that regulates further deformation, which is determined by the friction of rock-on-rock. Pre-fractured rocks, illustrated by the dashed curve, do not show this peak stress: they simply slide when the residual stress is reached.

As a rock sample is strained from its normal state, the rock responds first elastically then plastically. In the first regime, known as the elastic regime, the stress is directly proportional to strain. In most constitutive models, the maximum stress is assumed to occur at the elastic limit; that is, all strain up to the point of maximum stress is elastic and is recovered upon unloading. However, most rock mechanics experiments show that plastic deformation begins to occur slightly before the peak stress is reached (for example, see Jaeger and Cook 1969). Once the peak stress is reached, the rock sample begins to fail and damage accumulates. In this regime, known as the plastic regime, the deformation is permanent and is quantified by the plastic strain (the total strain is the sum of the elastic and plastic strains). The plastic strain required to deform an intact rock from the point where the stress is at a maximum until the residual stress is reached is called the equivalent plastic strain at failure. Just like the yield stress, this critical strain is a function of pressure, temperature, porosity, strain rate, and so on. For rocks subjected to tensile stresses, the equivalent plastic strain at failure is very small (<<0.01) because tensile failure is an unstable process. For compressive failure, the plastic strain at failure is typically 0.01–0.05, being larger for higher pressures.

A further complexity associated with brittle failure is the effect of porosity. Porous materials, when compressed, initially just compact with no associated rise in strength. Furthermore, when brittle materials fail, there is an associated increase in volume as new pores are created and rock fragments rearrange themselves to move over each other, known as bulking or dilatancy (Reynolds 1885). The volume of a rock mass undergoing bulking rises monotonically with increasing strain until the fragmented rock mass achieves a fully dilatant state and the bulk volume reaches a maximum. Compaction and bulking are difficult to implement into hydrocodes for simulating impact events because they affect both the constitutive model and the equation of state, which are usually treated separately.

As pressure increases, rocks respond to applied stress more and more homogeneously, and the difference between the strength of intact and damaged rocks becomes less significant. Such rocks are described as ductile. For ductile rocks, the concept of the plastic strain at failure loses its meaning as there is no stress drop associated with increasing plastic strain (see Fig. 1d). The brittle-ductile transition itself is of great interest in understanding the mechanics of earthquakes (Scholz 2002). Brittle faults near the Earth's surface broaden into shear zones at depths of many km. These zones contain sheared rocks such as mylonites. Recognizable shear zones ultimately disappear into broad regions of distributed deformation at the greatest depths. When strain rates are sufficiently high, ductile materials also undergo a kind of strain localization known as adiabatic shear bands (Gruntfest 1963). These shear bands are typically much broader than those that form in response in brittle failure. They arise in any material with resistance to flow that decreases as the temperature increases (Turcotte and Schubert 1982). Adiabatic shear bands could play an important role in the

deformation of the very deepest and hottest rocks surrounding truly gigantic impact craters but are not important for this discussion.

Note that the mode of failure and response of rock materials may well differ from the relatively low strain rate effects discussed and shown in Fig. 1 under shock and shock recovery conditions associated with impact events. Other processes may come into play in terms of how fractures are generated, how they evolve under conditions of supersonic compression and then rarefaction, and how the post-shock rock material behaves in the presence of large-amplitude high-frequency pressure fluctuations. Furthermore, there is much evidence that natural rock materials are much weaker on scales of tens to hundreds of m with respect to laboratory strength measurements of cm-scale rock samples (for example, Brune et al. 1993; Schmidt and Montgomery 1995). However, even at larger scales, the lower limit of rock strength must still be controlled by Coulomb's frictional law. The model we present here summarizes the current understanding of rock strength in the well-studied regime of geologic behavior.

The impact simulation shown here was performed using SALEB (Ivanov and Deutsch 1999; Ivanov and Artemieva 2002), a multi-material, multi-rheology extension of the SALE hydrocode (Amsden et al. 1980). SALEB is used in Eulerian mode, which means that the computational mesh is fixed and material flows through the mesh. The solution algorithm is similar to many other Eulerian hydrocodes in that, each timestep, the code calculates the displacement of each mesh vertex and then performs a remapping operation to flux material through the mesh according to the amount of overlap between the new and the old, fixed mesh. All cell-centered variables are fluxed through the mesh according to the volume of overlap across each cell boundary.

We incorporated a straightforward, yet sophisticated, constitutive model into SALEB that includes pressure and temperature dependent strength, shear and tensile failure, strain softening, both brittle and ductile deformation, and acoustic fluidization. A detailed description of our strength model, together with all the material parameters, is presented in the Appendix. The model presented here does not include the effect of porosity or bulking; however, we do discuss the potential implication of its inclusion. We show the results of 1 simulation, in 2D axial symmetry, as an illustrative example of what this detailed strength model implies for the state of the target during the impact in terms of strain and damage. The target material is granite of uniform composition. We use the ANEOS equation of state for granite together with constitutive model parameters based on the work of Lundborg (1968) and Stesky et al. (1974).

Damage and Deformation in an Impact Event

The details of how stresses and strains vary as an impact crater opens and then collapses are highly complex functions of many variables. Nevertheless, the impact simulation presented here gives a general overview of the stress and strain behavior through this process. Impact crater formation is broadly divided into 3 major stages: Contact and compression, excavation, and collapse (Melosh 1989). Contact and compression, the stage in which the kinetic energy of the projectile is transformed into heat and kinetic energy of the target, is irrelevant for discussions of damage and strain accumulation so long as the impact velocity exceeds a few km/sec. Most rocks undergo at least partial melting at shock pressures larger than ~50 GPa, a pressure that is exceeded in a basalt-on-basalt impact at a velocity of about 5.2 km/sec. Since most impacts in the solar system occur at much higher velocities (the average asteroidal impact velocity on Earth is 17 km/sec), we do not discuss this stage, although it is implicitly included in the numerical simulation.

The excavation stage includes both the expansion and dissipation of the shock wave and the opening of the crater cavity. Figure 2 shows the accumulation of damage during this stage of the simulated impact event. In our simulations, damage is a scalar, cell-centered quantity that reflects the totality of tensile and/or shear failure. In tension, a cell is considered to be completely damaged when flaw growth is sufficiently mature that the implied tensile cracks cross the width of the cell. In shear, total damage is achieved when the plastic strain is equal to the plastic strain at failure, which depends on the local pressure. Shear and tensile damage are combined by simple addition; the total damage is used to reduce both the tensile strength and shear strength. Thus, both processes may work on their own or in harmony. The frames of the impact simulation shown in Fig. 2 illustrate that both mechanisms contribute to the fracture state of the target rocks surrounding the crater. The left panel of each frame illustrates the extent of tensile failure; the right side illustrates the total damage due to both tensile and shear failure.

Shear failure is caused both by the passage of the compressive shock wave and by shear deformation during expansion of the transient cavity. It is controlled by 3 factors: 1) the decay of the shock wave with distance from the impact zone; 2) the increase in shear strength of rock material with increasing depth in the target; and 3) the changing style of deformation with depth, which is governed by the increase in plastic strain at failure with rising pressure. These effects combine to produce a gradual decrease in the amount of shear damage with depth below the crater, as can be seen in Fig. 2d. Strain localization during expansion of the shock wave leads to the finger-like extensions to the damaged zone in the brittle part of the target. Shear melting may occur on some fracture planes, resulting in the formation of melt veins known as pseudotachylites (Melosh 2003). Tensile failure occurs in the near-surface region, when the rarefaction wave releases the target rocks from the shock-induced high pressure, and beneath the crater floor, due to divergent crater growth flow and, especially, when the crater begins to rebound at the
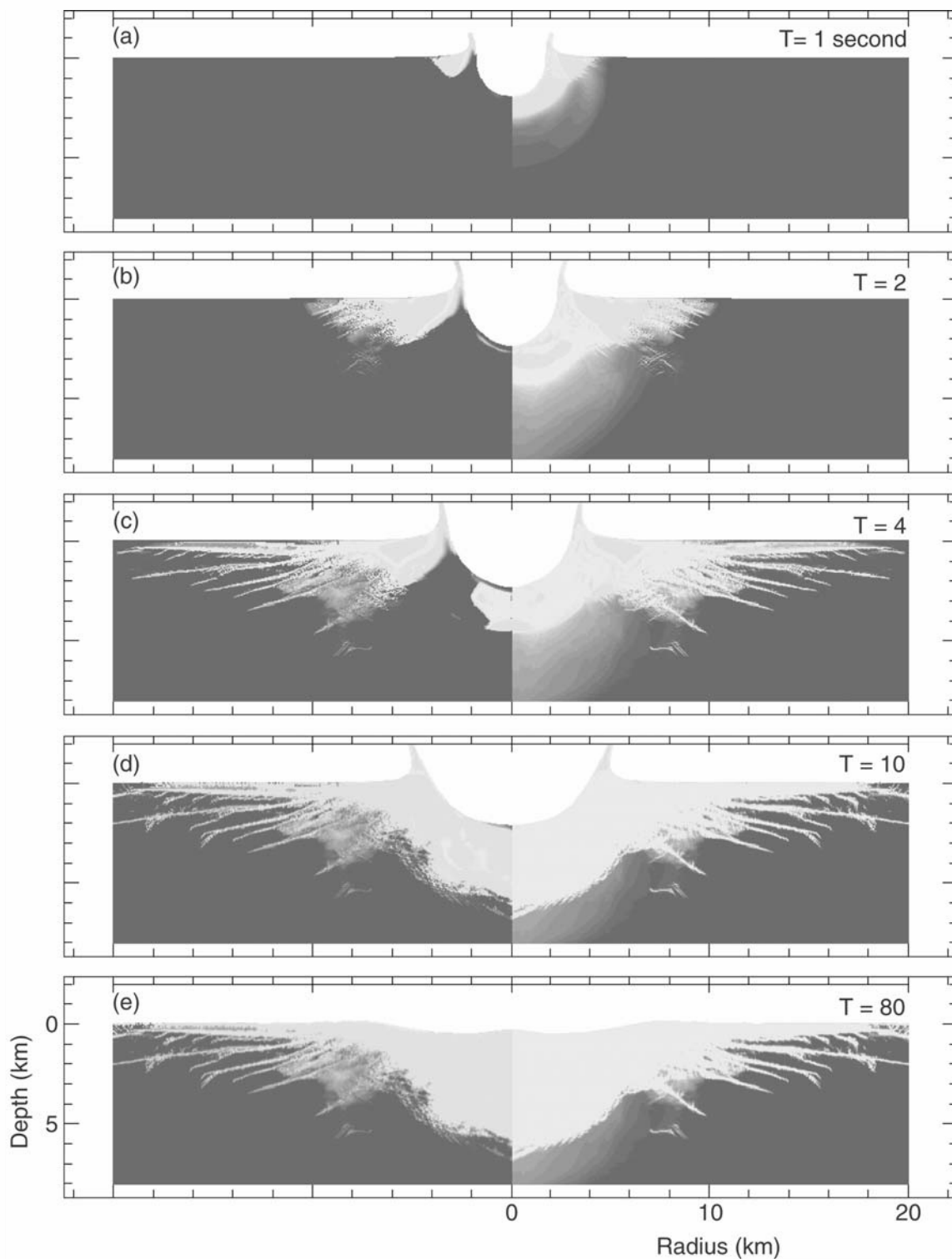
Fig. 2. Predicted damage contours from a simulation of a 10 km-diameter transient crater event at several times during the impact event. The left panel illustrates the tensile damage; the right side illustrates the combined shear and tensile damage. During the growth of the transient cavity (a–c), the damaged zone expands due to: 1) shear failure driven by the passage of the shock wave and the excavation flow; and 2) tensile failure induced by the release wave. During the transition between the outward excavation flow and the inward collapse flow, further tensile failure occurs beneath the crater floor as rebound begins (c–d). The final damaged region extends well away from the crater rim and floor, and is highly localized in the distal, brittle region of the target (e).

transition between the excavation stage and the collapse stage. As with shear failure, tensile damage is confined to the brittle near-surface zone; however, because tensile strength is not depth dependent, the transition from completely damaged to relatively undamaged material can be abrupt. During the complex motion of the sub-crater target material, incomplete shear failure may be completed by tensile failure and vice versa.

The shape and spacing of the damage contours are very sensitive to the constitutive model used. For softer rocks, which behave in a ductile manner at lower pressures, the brittle failure zone is smaller, and strain localization is not as pronounced; hence, ironically, the damaged zone is less extensive. For this reason, observations of disruption in the target surrounding a terrestrial crater from seismology and deep drill cores should provide a powerful validation for strength models used in impact simulations. The results presented here serve as an illustration of the predicted damage in a granitic target and cannot be directly extrapolated to craters formed in different target rocks.

The plastic strain experienced by a given material element in the target provides a quantitative measure of deformation induced by the impact event. In our simulations, we calculate two measures of plastic strain: the total plastic strain and the net plastic strain. We define the total plastic shear strain as the accumulated sum of plastic shear deformation, regardless of the sense of shear. The total plastic strain is calculated for each cell by adding an invariant measure of the plastic strain accumulated in the time step each cycle. Thus, the total plastic strain ε_{tot} is given by a sum over all time steps $n = 1$ to n_{tot}:

$$\varepsilon_{tot} = \sum_{n=1}^{n_{tot}} \dot{E}_n \Delta t_n \tag{1}$$

where Δt_n is the duration of the nth time step, and $\dot{E}_n$ is an invariant measure of the plastic strain rate in that step, defined in cylindrical coordinates by:

$$\dot{E}_n = \left(\frac{1}{6}[(\dot{\varepsilon}_{1,n} - \dot{\varepsilon}_{2,n})^2 + (\dot{\varepsilon}_{2,n} - \dot{\varepsilon}_{\theta,n})^2 + (\dot{\varepsilon}_{\theta,n} - \dot{\varepsilon}_{1,n})^2]\right)^{1/2} \tag{2}$$

where $\dot{\varepsilon}_{i,n}$ are the principal plastic strain rate components for the nth cycle. We define the net plastic strain as the overall amount of shear deformation, where the sense of shear is taken into account. Mathematically, the net plastic strain is defined as:

$$\varepsilon_{net} = \left(\frac{1}{6}[(\varepsilon_{xx} - \varepsilon_{yy})^2 + (\varepsilon_{yy} - \varepsilon_{\theta\theta})^2 + (\varepsilon_{\theta\theta} - \varepsilon_{xx})^2] + \varepsilon_{xy}^2\right)^{1/2} \tag{3}$$

where $\varepsilon_{ij} = \sum_{n=1}^{n=n_{tot}} \dot{\varepsilon}_{ij,n} \Delta t_n$ are the principal plastic strain components. Thus, the net plastic strain is equivalent to the standard geometric definition of shear strain in the case of simple shear in 2 dimensions:

$$\varepsilon_{net} = \int_0^t \dot{\varepsilon}_{xy} dt = \frac{1}{2}\int_0^t \left(\frac{dv}{dx} + \frac{du}{dy}\right) dt \tag{4}$$

where u and v are the velocities in the x and y direction respectively.

The difference between the total and net plastic strains, as we define them here, is most easily explained by consideration of 2-dimensional simple shear, where a square element is sheared by a horizontal stress (see Fig. 6) and then sheared back to its starting configuration (not shown in the figure). In this example, the net plastic strain increases from zero to a maximum, then the direction of the applied shear is reversed and the net plastic strain reduces back to zero. The total plastic strain, on the other hand, monitors the amount of deformation regardless of the sense of shear; hence, the total plastic strain is equal to twice the maximum net strain.

Figure 3 contours the total accumulated plastic shear strain (a) and final net plastic shear strain (b) around our simulated impact crater. These plots illustrate the intuitive result that the highest strains occur at the smallest radii. The innermost rocks, close to the impact site, always experience larger plastic strains than the more distant rocks. Within the damaged zone, the total plastic strains recorded during our simulation rise from ~0.01 at the damage zone boundary to ~3 near the crater (see Fig. 3a). However, only a small region of the target, close to the crater, experiences total plastic strains in excess of 1. The reversal in the direction of particle movements between the excavation flow and collapse flow implies that the net plastic strains experienced by the target are significantly less than the total plastic strains. Figure 3b illustrates that, although net plastic strains are still much greater nearer the crater, the magnitude of the net plastic strain are about a factor of 2 less than the total plastic strain.

The value of plastic strain may be visualized most easily in the context of a blocky media model. Consider two blocks of similar size that are displaced relative to one another within a shearing volume of rock fragments. In this simple model, a plastic strain of 0.01 corresponds to 1 block slipping over the other a distance 1/100 of its characteristic size. A plastic strain of 1, however, corresponds to a slip displacement comparable with the block size. Hence, at plastic strains of approximately 1, the original configuration of the rock fragments is lost; the rock pile loses its coherence. In reality, this conceptualization is complicated by the presence of a range of block sizes (see discussion below).

Figure 4 illustrates the deformational history of three regions of the simulated impact crater: 1) the central uplift region; 2) a region inside the crater rim and; 3) the region just outside the crater rim. Figure 4a shows typical particle paths for the material in these areas. The central uplift material (dash-dot curves) is depressed down during crater excavation
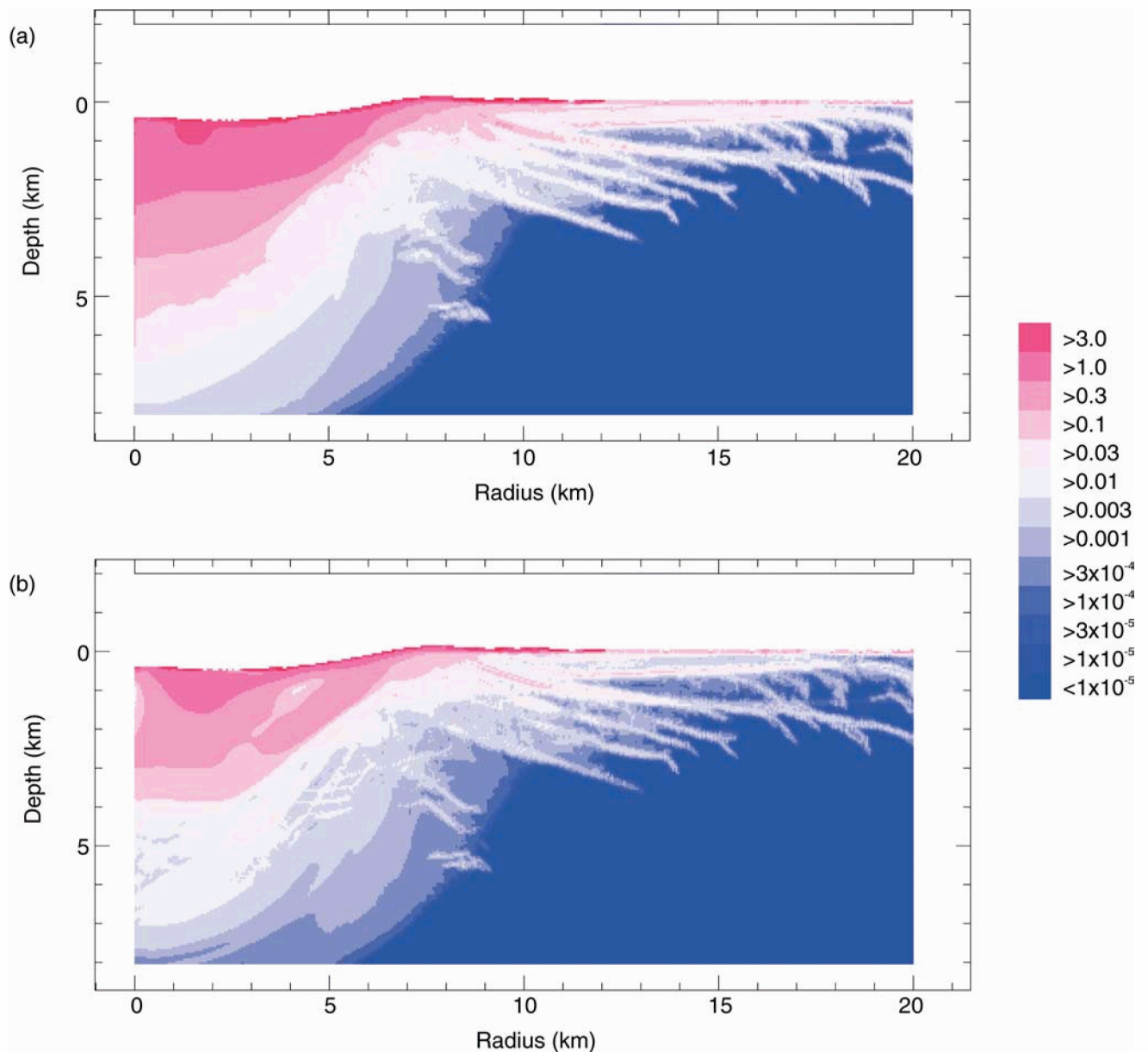
Fig. 3. Final strain contours from a simulation of a 10 km-diameter transient crater event: a) total accumulated plastic strain; b) net plastic strain.

and is then pushed back up by the collapse flow. As this region is the closest to the impact site of the 3 depicted, this region experiences the highest strain rates, illustrated by the steepest rise in strain (Figs. 4b and 4c), and a large total plastic strain (see Fig. 4b). The net plastic strain in the central uplift is significantly less than this due to the reversal in sign of the strain when excavation turns into collapse after ~15 sec (Fig. 4c). The target material between the central uplift and the crater rim (dashed curves) is pushed outward and upward during excavation and then returned along similar trajectories during collapse. Consequently, the dashed curves illustrate similar plastic strain histories (Fig. 4c); however, the total

plastic strain accumulated is less far away from the crater (Fig. 4b). The region of the target immediately outside the final crater rim (solid curves) is not involved in the collapse flow (Fig. 4a). Hence, the total plastic strain and net plastic strain accumulated in this region are equivalent and much less than the plastic strain experienced by material displaced during the collapse flow.

It may appear that the damage and plastic strain plots (Figs. 2e and 3a) illustrate homogeneous damage and plastic strain over large regions of the target surrounding the crater. However, continuum modeling requires care in the interpretation. Time and computing constraints limited the
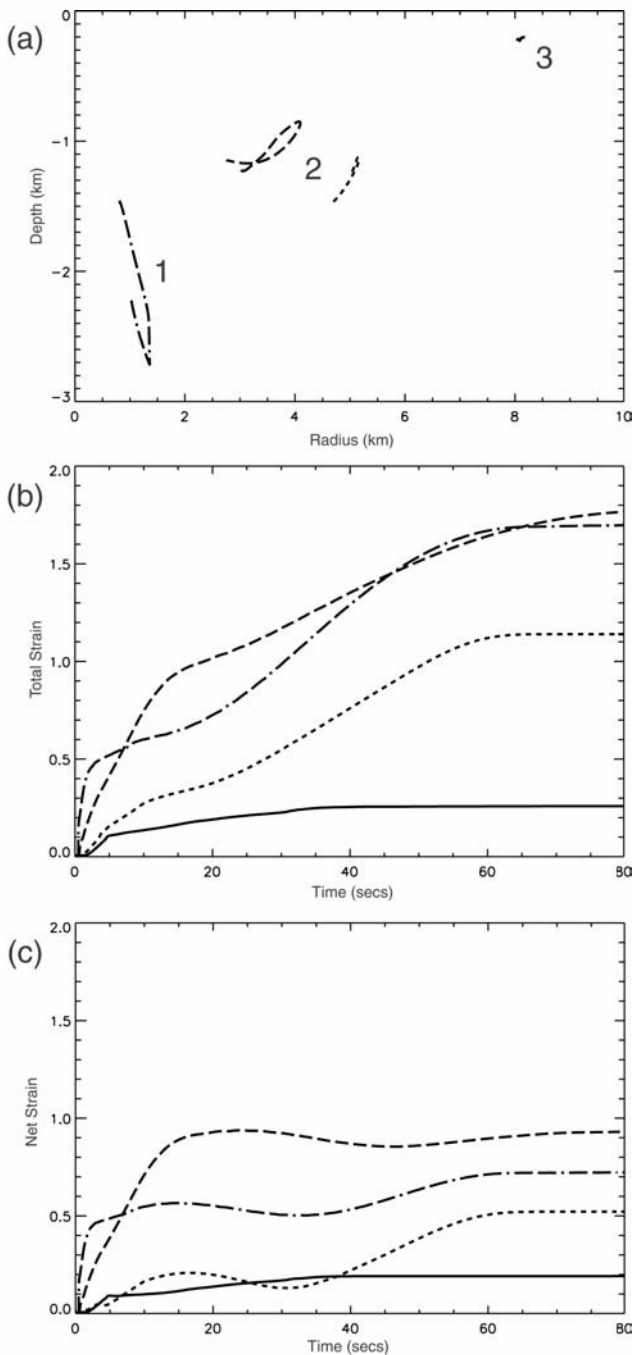
Fig. 4. Displacement and strain histories for three different regions of the target: a) particle motions; b) total plastic strain; c) net plastic strain.

minimum cell size in the simulation discussed here to 50 × 50 m. Thus, by its very nature, our numerical model simulates all deformation in terms of an average strain that applies over this scale. The damage and strain on scales smaller than this must be left to interpretation based on the failure regime (brittle/ductile) and, hence, the pressure and temperature history.

To illustrate this point, we performed two simulations of simple shear where we forced a volume of rock material to deform at an approximately constant pressure and constant strain rate within the brittle deformation regime. One of the simulations comprised a mesh of 1 cell; the other was 100 × 100 cells. The stress-strain behavior of the single-cell mesh is shown in Fig. 5, which mimics the stress-strain curve for brittle rock in compression, shown in Fig. 1. As deformation increases, the stress rises to a peak at a strain of 0.01 and then declines as shear failure occurs and plastic strain accumulates. By the time the shear strain has reached 0.05, the cell is completely damaged, implying that the shear strength of the cell is that of completely fractured rock material (simple Coulomb friction). Figure 6 shows damage contours at four times during an identical simulation, except with 10000 cells. In comparison with the single-cell mesh, where the cell dimensions are 100 × 100 m, we now have a resolution of 1 × 1 m (still large compared to a typical hand specimen). At a strain of 0.015 (Fig. 6a), this higher resolution simulation shows a single crack through the rock volume. By the time the average shear strain over the whole volume is 0.05 (Fig. 6c), several cracks have developed and the rock volume can be considered to comprise several smaller intact fragments. Thus, it seems valid that the bulk strength of the rock volume should be considered to be that of a cohesionless rock mass, as is the case in the low resolution simulation at the equivalent strain. However, when analyzed on a fine scale, the strain in the high resolution simulation is localized and the deformation is discrete, with some portions of the rock volume remaining intact out to large strains.

The central point demonstrated by these two simulations is that, because strain in brittle rocks is very heterogeneous, the results of continuum modeling of impact events must be interpreted with care. The models describe the deformation of the target during an impact event in terms of an average strain that applies over a large volume of rock (large compared to the spacing between individual zones of sliding). Smaller-scale damage and deformation, however, will likely be localized. All that the models can predict is a bulk strain and damage, with which the finer-scale strain should be consistent. Also not modeled here are more irregular motions that may result in the relative rotations of blocks and mixing of fractured material. At the moment, such details are beyond the scope of numerical modeling, although they are often observed in the field.

The relation between the average strain (e), and the displacement along a given fracture zone (d), is determined by a quantity with the dimension of length. A simple relation links the displacement and strain:

$$d = Le \tag{5}$$

The dimension (L) may be either the fracture length or the average spacing between fractures (these two are usually nearly the same numerically, as parallel fractures relieve differential stresses to distances comparable to their own length; Lachenbruch 1961). In any real mass of rock,
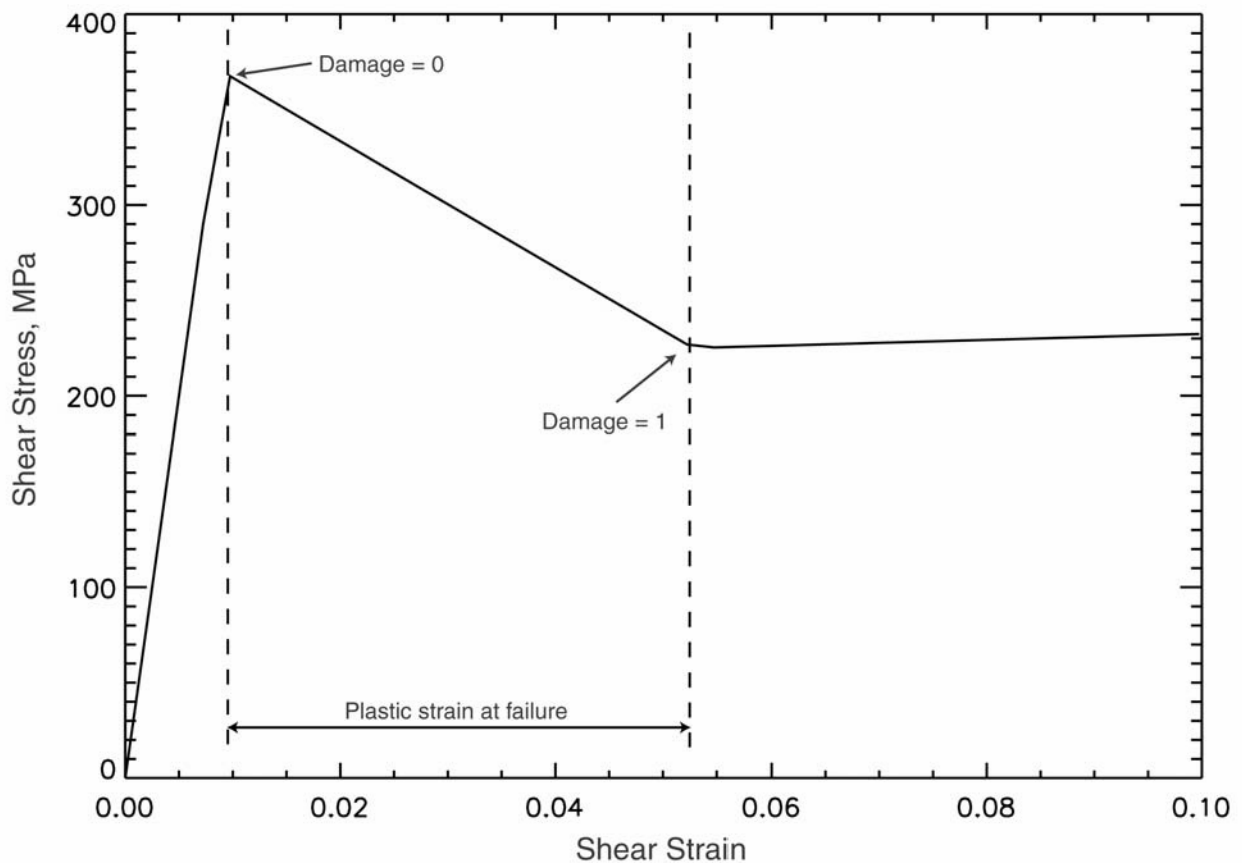
Fig. 5. Stress-strain curve for a numerical simple-shear experiment involving 1 cell. During the simulation, the cell is sheared at a constant strain rate. The stress rises monotonically with increasing strain to a maximum at ~0.01. During this phase, the deformation is elastic and no damage accumulates (D = 0). With increasing strain, damage starts to accumulate and deformation is permanent—further strain is "plastic." At a total strain of ~0.05, when the plastic strain reaches the "plastic strain at failure," damage is total (D = 1). From this point onwards, the strength of the cell is constant, controlled by the friction of rock-on-rock. (Note: the slight rise in stress with increasing strain is due to a slight increase in pressure during the numerical simulation. Unfortunately, the cell could not be kept at an exactly constant pressure throughout the calculation.)

multiple length scales are likely to be present, and a full analysis must sum over all these scales in some way. For example, in a region with an average strain of 0.03, this could be the cumulative result of a 3 mm displacement on small fractures spaced 10 cm apart or of 30 cm offsets on faults spaced 10 m apart. The average strain concept does not specify the size scale (L), which must, therefore, be determined by other considerations. Joints are universal in crustal rocks, and it would be tempting to equate (L) with the spacing of pre-existing joint sets. However, due to limitations on the ability of pre-existing joints to accommodate arbitrary strains, it seems inevitable that new fractures must form in any large impact event. Perhaps a useful field measurement for comparison with the numerical models, therefore, would be to identify displacements, and the separations between these displacements, on a range of scales and then estimate the average strain over the field area using Equation 5.

A secondary result illustrated by the high resolution simulation of simple shear is that the fracture density within the deforming rock mass is also related to strain. Hence, if the effects of bulking were included in this simulation, the shear deformation would also result in a reduction in bulk density with increasing strain. This suggests that strain maps produced by numerical simulations can be used to identify regions of pervasive fracturing, intense brecciation, and, hence, low density and low seismic velocity. In the impact simulation presented here, the target in close proximity to the crater is all strained to approximately the same high degree (Fig. 3). Thus, it is in this region that we would expect to see the largest fracture density, the smallest-sized breccia material, the lowest bulk density, and the lowest seismic velocity. For larger peak ring craters, we would expect the peak ring material, which experiences the most strain, to be the most fractured/brecciated. The peak ring,
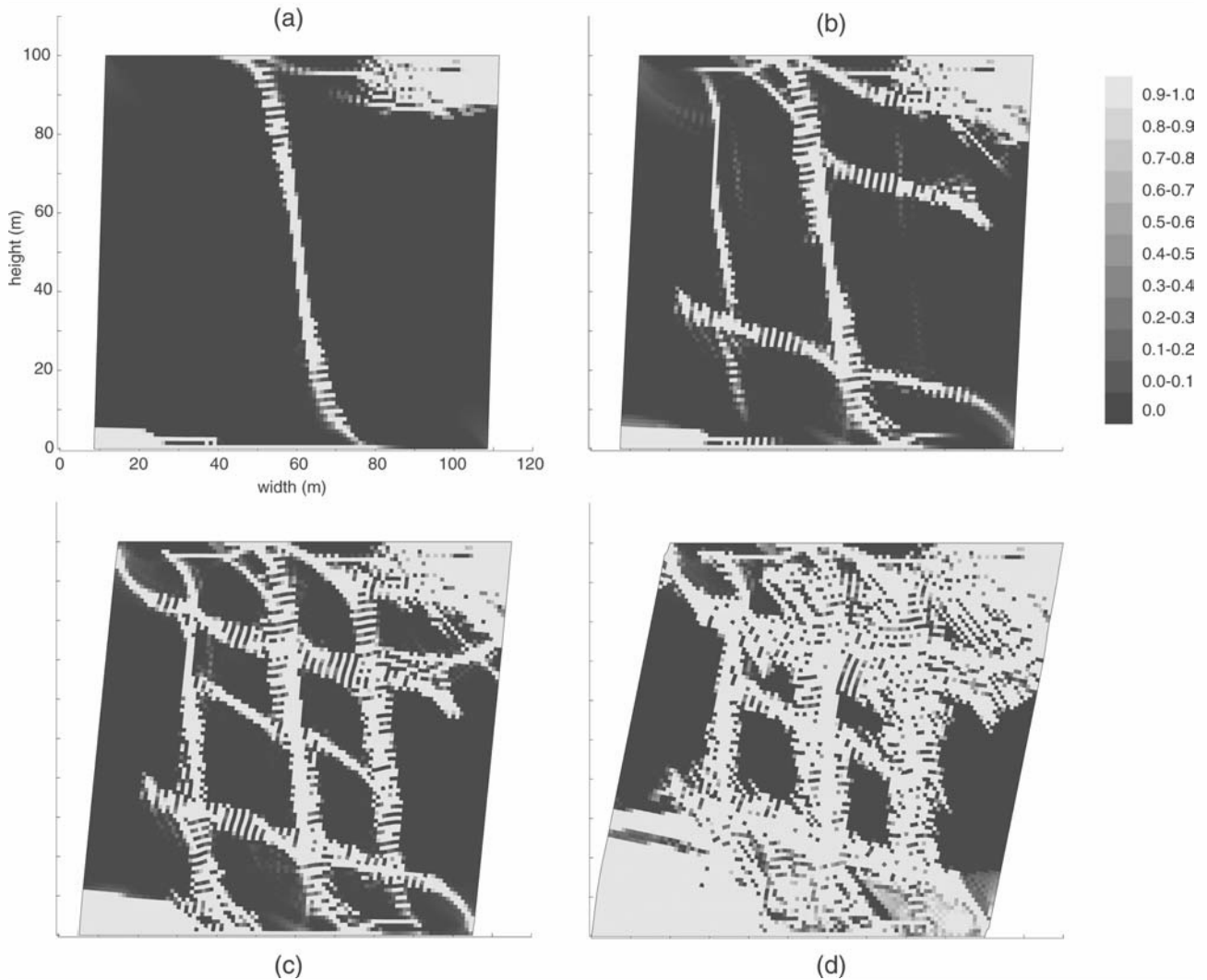
Fig. 6. Fracturing observed in a high resolution numerical simulation of simple shear. In this calculation, the mesh resolution was 100×100 cells, compared to 1 cell in Fig. 5. During the simulation, the mesh is sheared at the same constant strain rate as in the low resolution calculation. Shown are contour plots of damage at 4 different times, which correspond to strains of: a) 0.015 (1.5%); b) 0.025 (2.5%); c) 0.05 (5%); and d) 0.1 (10%). At this resolution, brittle failure leads to strain localization not uniform failure throughout the mesh. Fracture density increases and intact fragment size decreases with increasing strain.

therefore, should be a region of relatively low bulk density and low seismic velocity. In the case of Chicxulub, this result is consistent with gravity observations (Pilkington et al. 1994) and seismic tomography (Morgan et al. 2000).

CONCLUSIONS

Numerical modeling is a powerful tool for investigating the formation of large impact craters. However, it is unwise to draw conclusions based on numerical simulations without the validation of model results by observational evidence. Quantitative analysis of damage and deformation in the target surrounding an impact event could provide a good means of validation for numerical models of terrestrial impact craters,

particularly in cases where the final pristine crater morphology is ambiguous or unknown.

The failure of brittle materials is complicated and requires a sophisticated constitutive model to simulate. We use such a model to simulate a mid-sized impact into a granitic terrestrial crust. The results from this simulation illustrate the typical deformational response of a planetary target to an impact event where stresses, strains, and strain rates are all highest near the impact site and decrease with radial distance. The reversal in flow patterns from the downward and outward excavation flow to the inward and upward collapse flow implies that net plastic strains may be significantly lower than total plastic strains.

Strain in brittle rocks is very heterogeneous. However, continuum modeling requires that the deformation of the target

during an impact event be described in terms of an average strain that applies over a large volume of rock (large compared to the spacing between individual zones of sliding). This paper demonstrates that model predictions of smooth average strain are entirely consistent with an actual strain concentrated along very narrow zones. Furthermore, we suggest that model predictions of total accumulated strain should correlate with observed variations in bulk density and seismic velocity. We hope that this short demonstration will inspire modelers and observers alike to take a detailed, quantitative look at damage and deformation in terrestrial impact craters.

Editorial Handling—Dr. E. Pierazzo and Dr. R. Herrick

REFERENCES

Amsden A. A., Ruppel H. M., and Hirt C. W. 1980. SALE: A simplified ALE computer program for fluid flows at all speeds, LA-8095 Report. Los Alamos: Los Alamos National Laboratories. 101 p.

Ashby M. F. and Sammis C. G. 1990. The damage mechanics of brittle solids in compression. *Pure and Applied Geophysics* 133: 489–521.

Bjork R. L. 1961. Analysis of the formation of Meteor Crater, Arizona. A preliminary report. *Journal of Geophysical Research* 66:3379–3387.

Bombolakis E. G. 1973. Study of the brittle fracture process under uniaxial compression. *Tectonophysics* 18:231–248.

Brune J. N., Brown S., and Johnson P. A. 1993. Rupture mechanism and interface separation in foam rubber models of earthquakes: A possible solution to the heat flow paradox and the paradox of large overthrusts. *Tectonophysics* 218:59–67.

Byerlee J. 1978. Friction of rocks. *Pure and Applied Geophysics* 116: 615–626.

Collins G. S., Melosh H. J., Morgan J. V., and Warner M. R. 2002. Hydrocode simulations of Chicxulub crater collapse and peak-ring formation. *Icarus* 157:24–33.

Dence M. R., Grieve R. A. F., and Robertson P. B. 1977. Terrestrial impact structures: Principal characteristics and energy considerations. In *Impact and explosion cratering,* edited by Roddy D. J., Pepin R. O., and Merrill R. B. New York: Pergamon Press. pp. 247–275.

Evans B. and Kohlstedt D. L. 1995. Rheology of rocks. In *Rock physics and phase relations: A handbook of physical constants,* edited by Ahrens T. J. Washington D.C.: American Geophysical Union. pp. 148–165.

Goetze C. 1978. The mechanism of creep in olivine. *Philosophical Transactions of the Royal Society of London A* 288:59–119.

Grieve R. A. F., Dence M. R., and Robertson P. B. 1977. Cratering processes: As interpreted from the occurrence of impact melts. In *Impact and explosion cratering,* edited by Roddy D. J., Pepin R. O., and Merrill R. B. New York: Pergamon Press. pp. 791–814.

Grieve R. A. F., Robertson P. B., and Dence M. R. 1981. Constraints on the formation of ring impact structures, based on terrestrial data. In *Multi-ring basins: Formation and evolution,* edited by Schultz P. H. and Merrill R. B. New York: Pergamon Press. pp. 37–59.

Gruntfest I. J. 1963. Thermal feedback in liquid flow: Plane shear at constant stress. *Transactions of the Society of Rheology* 7:195–207.

Horii H. and Nemat-Nasser S. 1986. Brittle failure in compression: Splitting, faulting, and brittle-ductile transition. *Philosophical Transactions of the Royal Society of London A* 31:337–374.

Ivanov B. A. 2002. Deep drilling results and numerical modeling: Puchezh-Katunki impact crater, Russia (abstract #1286). 33rd Lunar and Planetary Science Conference. CD-ROM.

Ivanov B. A., Deniem D., and Neukum G. 1997. Implementation of dynamic strength models into 2D hydrocodes: Applications for atmospheric break-up and impact cratering. *International Journal of Impact Engineering* 17:375–386.

Ivanov B. A. and Artemieva N. A. 2002. Numerical modeling of the formation of large impact craters. In *Catastrophic events and mass extinctions: Impact and beyond.* Special Paper 356. Washington D.C: Geological Society of America. pp. 619–630.

Ivanov B. A. and Deutsch A. 1999. Sudbury impact event: Cratering mechanics and thermal history. In *Large meteorite impacts and planetary evolution II,* edited by Dessler B. and Grieve R. A. F. Special Paper 339. Washington D.C.: Geological Society of America. pp. 389–397.

Ivanov B. A. and Kostuchenko V. N. 1997. Block oscillation model for impact crater collapse (abstract #1655). 27th Lunar and Planetary Science Conference. CD-ROM.

Johnson G. R. and Holmquist T. J. 1993. An improved computational constitutive model for brittle materials. In *High-pressure science and technology: 1993,* edited by Schmidt S. C., Shaner J. W., Samara G. A., and Ross M. Woodbury: AIP Press. pp. 981–984.

Jaeger J. C. and Cook N. G. W. 1969. *Fundamentals of rock mechanics.* London: Chapman and Hall.

Lachenbruch A. H. 1961. Depth and spacing of tension cracks. *Journal of Geophysical Research* 66:4273–4292.

Lambert P. 1981. Breccia dikes: Geological constraints on the formation of complex craters. In *Multi-ring basins: Formation and evolution,* edited by Schultz P. H. and Merrill R. B. New York: Pergamon Press. pp. 59–78.

Lockner D. A. 1995. Rock failure. In *Rock physics and phase relations: A handbook of physical constants,* edited by Ahrens T. J. Washington D.C.: American Geophysical Union. pp. 127–147.

Lundborg N. 1968. Strength of rock-like materials. *International Journal of Rock Mechanics and Mining Sciences* 5:427–454.

Melosh H. J. 1979. Acoustic fluidization: A new geologic process? *Journal of Geophysical Research* 84:7513–7520.

Melosh H. J. 1989. *Impact cratering: A geologic process.* New York: Oxford University Press. 245 p.

Melosh H. J. 2003. Mechanics of pseudotachylite formation during impact events. Proceedings, 2002 Impact Tectonism Workshop.

Melosh H. J. and Ivanov B. A. 1999. Impact crater collapse. *Annual Review of Earth and Planetary Sciences* 27:385–415.

Melosh H. J., Ryan E. V., and Asphaug E. 1992. Dynamic fragmentation in impacts: Hydrocode simulation of laboratory impacts. *Journal of Geophysical Research* 97:14735–14759.

Morgan J. V., Warner M. R., Collins G. S., Melosh H. J., and Christeson G. L. 2000. Peak-ring formation in large impact craters. *Earth and Planetary Science Letters* 183:347–354.

Ohnaka M. 1995. A shear failure strength law of rock in the brittle-plastic transition regime. *Geophysical Research Letters* 22:25–28.

O'Keefe J. D. and Ahrens T. J. 1993. Planetary cratering mechanics. *Journal of Geophysical Research* 98:17011–17028.

O'Keefe J. D. and Ahrens T. J. 1999. Complex craters: Relationship of stratigraphy and rings to the impact conditions. *Journal of Geophysical Research* 10:27091–27104.

O'Keefe J. D., Stewart S. T., Lainhart M. E., and Ahrens T. J. 2001. Damage and rock-volatile mixture effects on impact crater formation. *International Journal of Impact Engineering* 26:543–553.

Pilkington M., Hildebrand A. R., and Ortiz-Aleman C. 1994. Gravity and magnetic field modeling and structure of the Chicxulub crater, Mexico. *Journal of Geophysical Research* 99:13147–13162.

Poirier J. P. 1994. Plastic rheology of crystals. In *Mineral physics and crystallography: A handbook of physical constants,* edited by Ahrens T. J. Washington D.C.: American Geophysical Union. pp. 237–247.

Reynolds O. 1885. On the dilatancy of media composed of rigid particles in contact. With experimental illustrations. *Philosophical Magazine Letters* 20:469–549.

Rice J. R. 1976. The localization of plastic deformation. Proceedings, 14th International Congress of Theoretical and Applied Mechanics. pp. 207–220.

Rubin M. B., Vorobiev O. Y., and Glenn L. A. 2000. Mechanical and numerical modeling of a porous elastic-viscoplastic material with tensile failure. *International Journal of Solids and Structures* 37:1841–1871.

Scholz C. H. 2002. *The mechanics of earthquakes and faulting.* Cambridge: Cambridge University Press. p. 471.

Schmidt K. M. and Montgomery D. R. 1995. Limits to relief. *Science* 270:617–620.

Spray J. G. 1998. Localized shock- and friction-induced melting in response to hypervelocity impact. In *Meteorites: Flux with time and impact effects,* edited by Grady M. M., Hutchison R., McCall G. J. H., and Rotherby D. A. Special Publication 140. London: Geological Society. pp. 171–180.

Stesky R. M., Brace W. F., Riley D. K., and Bobin P. Y. 1974. Friction in faulted rock at high temperature and pressure. *Tectonophysics* 23:177–203.

Turcotte D. L. and Schubert G. 1982. *Geodynamics: Applications of continuum physics to geological problems.* New York: John Wiley & Sons. 464 p.

Wünnemann K and Ivanov B. A. 2003. Numerical modelling of the impact crater depth-diameter dependence in an acoustically fluidized target. *Planetary and Space Science* 51:831–845.

APPENDIX: CONSTITUTIVE MODEL

The complexity involved with accurately simulating impact events to late stages resides in how to prescribe the appropriate yield strength for a given cell of material in the target. In the past, the yield strength has often been defined to be independent of pressure, strain, or strain rate or to be a simple function of internal energy, such that it vanishes at the melting point. However, the strength of rock materials is far more complicated. Rock mechanics experiments show that the critical stress at the onset of failure is a function of confining pressure, temperature, strain rate, porosity, and sample size. Furthermore, brittle materials show two distinct types of failure mechanism: tensile failure and shear failure. The following discussion details the constitutive model used in the simulations presented in this paper. The formulation and implementation of the following constitutive equations in SALEB are the result of many years work by Boris Ivanov (see, for example, Ivanov et al. 1997) and recent collaboration with Gareth Collins and Jay Melosh. The constitutive model parameters used for the simulations presented here appear in Table A1.

Shear Failure

SALEB treats the target as an elastic-plastic (or viscoelastic-plastic) solid. This means that the rheologic stress in a given cell is linearly related to the strain, for stresses below the yield stress, or strength. Above this yield stress, the material behaves plastically, in the sense that deformation is permanent, and the stress is limited by the yield stress. The procedure for implementing this scheme is to compare an invariant measure of stress in a cell with the prescribed yield stress. The stress invariant used in SALEB is the second invariant of the deviatoric stress tensor J_2, given by:

$$J_2 = \frac{1}{6}[(\sigma_{e1} - \sigma_{e2})^2 + (\sigma_{e1} - \sigma_{e\theta})^2 + (\sigma_{e\theta} - \sigma_{e1})^2] \tag{A1}$$

where σ_{ei} are the elastic principal stresses in cylindrical coordinates. The elastic principal stresses are computed from the elastic deviatoric stresses, which are defined by the elastic deviatoric strain components. These are updated each time step by first assuming that all deformation is elastic. If J_2 exceeds the square of the yield strength (Y), then shear failure has occurred: the updated elastic deviatoric stress components (and deviatoric elastic strain components) must be reduced to the yield envelope by multiplying by the factor $Y/\sqrt{J_2}$. The remaining strain (the difference between the elastic deviatoric strain components before and after the yield correction is applied) is the plastic strain. We record the plastic strain both in component form for computation of the net plastic strain and as a sum of an invariant measure of the plastic strain increment for computation of the total plastic strain (see below).

To approximate the effect of pressure on yield strength for intact rock (Y_i), we use a smooth approximation to experimental data first defined by Lundborg (1968):

$$Y_i = Y_0 + \frac{\mu_i p}{1 + \mu_i p/(Y_M - Y_0)} \tag{A2}$$

where Y_0 is the shear strength at zero pressure, μ_i is the coefficient of internal friction, and Y_M is known as the von Mises plastic limit of the material.

For completely fragmented rock material, we use a Coulomb dry-friction law. In this case, the yield strength is given by:

$$Y_d = \mu_d p \tag{A3}$$

where μ_d is the coefficient of friction for the damaged

material. This relationship is only valid for confining pressures where $Y_d < Y_i$; at pressures above this, the shear strength follows the same pressure dependence given by Equation A2, regardless of damage.

For partially fragmented material, a quantity called "damage" D is defined, which takes a value of between 0 for completely undamaged and 1 for totally damaged material. The damage quantity may then be used to define intermediate yield strengths according to the equation (after Ivanov et al. 1997):

$$Y = (1 - D)Y_i + DY_d \qquad (A4)$$

Damage may be accumulated due to shear deformation or tensile failure. Here, we separate the two mechanisms and define the total damage (D) as the sum of the tensile damage D_t, which will be discussed in the next section, and the shear damage D_s. Following the scheme of Johnson and Holmquist (1993), among others, we define the shear damage as the integrated plastic strain ε_{tot} divided by the accumulated plastic strain at the point of failure ε_f, which is known to be a function of pressure, temperature, and material type:

$$D_s = \min\left(1, \frac{\varepsilon_{tot}}{\varepsilon_f}\right) \qquad (A5)$$

The integrated plastic strain is calculated by adding an invariant measure of the plastic strain accumulated in the time step each cycle. Thus, the total plastic strain (ε_{tot}) is given by a sum over all time steps $n = 1$ to n_{tot}:

$$\varepsilon_{tot} = \sum_{n=1}^{n_{tot}} \dot{E}_n \Delta t_n \qquad (A6)$$

where Δt_n is the duration of the nth time step and $\dot{E}_n$ is an invariant measure of the plastic strain rate in that step, defined in cylindrical coordinates by:

$$\dot{E}_n = \left(\frac{1}{6}[(\dot{\varepsilon}_{1,n} - \dot{\varepsilon}_{2,n})^2 + (\dot{\varepsilon}_{2,n} - \dot{\varepsilon}_{\theta,n})^2 + (\dot{\varepsilon}_{\theta,n} - \dot{\varepsilon}_{1,n})^2]\right)^{\frac{1}{2}} \quad (A7)$$

where $\dot{\varepsilon}_{i,n}$ are the principal plastic strain rate components for the nth cycle.

To define the plastic strain required for complete failure, we adopt the philosophy presented in Evans and Kohlstedt (1995) where shear failure occurs within one of three regimes: brittle, semi-brittle, and plastic, depending on the confining pressure (see Fig. 1). For low confining pressures, where the strength of the damaged material is less than that for intact specimens ($Y_d < Y_i$), the plastic strain at failure rises from 0.01 at zero pressure, to 0.05 at the brittle-ductile transition pressure (p_{bd}). In this regime, rock failure is by discrete brittle failure along microcracks. Failure occurs after minimal plastic strain, and the strength drop due to damage is significant. Hence, strong strain localization is expected. In stark contrast, for very

large confining pressures, where the pressure is greater than twice the shear strength ($p > 2Y$), rock behaves plastically (Goetze 1978). In this case, deformation results not from crack growth or frictional slip but from motion of point defects, dislocations, and twins or from grain boundary sliding (Poirier 1994). Furthermore, the yield strength does not drop with increasing plastic strain. In this regime, we define the plastic strain at failure to rise abruptly from 0.1 at the brittle-plastic transition pressure (p_{bp}) to 1 at twice the brittle-plastic transition pressure. In the semi-brittle regime, which lies in the pressure range $p_{bd} < p < p_{bp}$, we define the plastic strain at failure to rise linearly from 0.05–0.1. This reflects the deformation regime that includes both brittle fracture and ductile flow. Rock deforming in this regime will show signs of brittle failure, however, the damage has no effect on the yield strength.

The shear strength of rock materials also depends on temperature (see, for example, Jaeger and Cook 1969). As the material approaches the melting temperature, the shear strength drops off to zero at the melting temperature. We approximate this behavior using the simple relationship (after Ohnaka 1995):

$$Y_t = Y \tanh\left[\xi\left(\frac{T_m}{T} - 1\right)\right] \qquad (A8)$$

where T and T_m are the ambient and melt temperature, respectively, and ξ is a material constant.

The complete shear strength algorithm is as follows. The shear strength of the material in the cell is determined based on the current pressure, temperature, and damage. The stress in the cell is calculated assuming that all the strain can be accommodated elastically. If this stress exceeds the yield strength, the elastic stresses and strains are reduced and the remaining strain is accommodated plastically. This plastic strain is recorded and used to determine the shear damage by dividing it by the plastic strain at failure, which is a function of pressure. The total damage in the cell to be used in the subsequent time step is this shear damage plus any tensile damage that may have accumulated. Tensile failure is the topic of the next section.

Tensile Failure

At low confining pressures, where one of the principal stress components is tensile, brittle failure of rock takes on a distinctly different form to that described in the previous section. In the case of tensile failure, once the tensile strength of rock is exceeded, flaws in the sample tend to grow in the direction perpendicular to the maximum tension axis. These flaws concentrate the applied stress at their tips, thus increasing the effective stress across the remaining intact rock. Consequently, the development of these flaws perpetuates their own growth, resulting in a rapid, unstable path to complete failure. For this reason, tensile failure is said to be unstable.

One possible method for treating tensile failure is to simply extrapolate the shear failure envelope shown in Fig. 1 to negative pressures and limit the minimum pressure by the tensile strength of rock materials as measured in the laboratory. In addition, the plastic strain at failure in this regime could be set to some small strain to reflect the fact that tensile failure is rapid and an almost instantaneous response once the yield envelope is exceeded. However, due to the clear distinction between the physical mechanisms involved in shear and tensile failure, we prefer to adopt a different approach and to calculate tensile failure separately.

For purely Lagrangian computer codes, an attractive algorithm is the Grady-Kipp-Melosh model of tensile failure (Melosh et al. 1992). However, for Eulerian simulations, the implementation of this model is complex; consequently, we have developed a simple, single-flaw-growth model, which approximates the approach of the Grady-Kipp-Melosh model in the low strain-rate limit. In this model, we calculate the most tensile post-shear-failure principal elastic stress in the cell and compare it to the current tensile strength of the cell. If the tensile stress exceeds the tensile strength, we reduce the elastic stresses accordingly and compute the growth of a single flaw in the cell, assuming that the flaw grows at the crack-growth speed (c_g). The tensile damage in the cell is given formally by the equation:

$$\frac{dD_t^{1/3}}{dt} = \frac{c_g}{\min(dx, dy)} \tag{A9}$$

where dx and dy are the dimensions of the cell. The tensile damage is added to the shear damage to give the total damage; this combined damage is then used to modify the tensile strength of the cell.

Acoustic Fluidization

To facilitate complex crater collapse we also include the effect of transient, high-frequency pressure oscillations in the target surrounding the impact point. These pressure fluctuations modify the frictional strength of the damaged target by temporarily reducing the overburden pressure and, hence, allowing temporally and spatially localized slip between rock fragments. The time- and space-averaged result of these small-scale slip events is that the rock mass takes on a fluid-like rheology from a macroscopic point of view. This process is known as acoustic fluidization (Melosh 1979). The acoustic fluidization algorithm implemented in SALEB follows the "block-model" approximation of Ivanov and Kostuchenko (1997). The algorithm is discussed in detail in Melosh and Ivanov (1999).

Table A1. Parameter definitions and values used in all numerical simulations.

Parameter	Definition	Value used
Y_0	Cohesion (yield strength at zero pressure)	90 MPa
Y_m	von Mises plastic limit (yield strength at infinite pressure)	1.5 GPa
μ_i	Coefficient of internal friction	2.0
μ_d	Coefficient of friction	0.8
T_m	Melt temperature	1500 °K
ξ	Thermal softening parameter	1.2
P_{bd}	Brittle-ductile transition pressure	1.23 GPa
P_{bp}	Brittle-plastic transition pressure	2.35 GPa
Y_T	Tensile strength	10 MPa
c_g/c_s	Crack-growth speed/bulk sound speed	0.5